1  **Experimental constraints on melting temperatures in the MgO-SiO$_2$ system at**

2  **lower mantle pressures**

3

4  Marzena A. Baron[a,b*], Oliver T. Lord[b], Robert Myhill[b], Andrew R. Thomson[b,c], Weiwei

5  Wang[b,c], Reidar G. Trønnes[a,d], Michael J. Walter[b]

6

7  a – Centre for Earth Evolution and Dynamics (CEED), University of Oslo, P.O. Box 1028

8      Blindern, Oslo, N-0315, Norway.

9  b – School of Earth Sciences, University of Bristol, Wills Memorial Building, Queens's

10      Road, Bristol, BS8 1RJ, UK.

11  c – Department of Earth Sciences, University College London, Gower Street, London,

12      WC1E 6BT, UK.

13  d – Natural History Museum, University of Oslo, P.O. Box 1172 Blindern, Oslo, N-0318,

14      Norway.

15

16  **Keywords:** lower mantle; eutectic melting; diamond anvil cell; Early Earth Evolution;

17          basalt; peridotite.

18

19

20

21

22

23

24

25

* Corresponding author:
 Marzena Anna Baron - Tel: +47 22 85 62 54
 E-mail address: m.a.baron@geo.uio.no / marzena.a.baron@gmail.com

**Abstract**

Eutectic melting curves in the system $MgO$-$SiO_2$ have been experimentally determined at lower mantle pressures using laser-heated diamond anvil cell (LH-DAC) techniques. We investigated eutectic melting of bridgmanite plus periclase in the $MgO$-$MgSiO_3$ binary, and melting of bridgmanite plus stishovite in the $MgSiO_3$-$SiO_2$ binary, as analogues for natural peridotite and basalt, respectively. The melting curve of model basalt occurs at lower temperatures, has a shallower $dT/dP$ slope and slightly less curvature than the model peridotitic melting curve. Overall, melting temperatures detected in this study are in good agreement with previous experiments and *ab initio* simulations at ~25 GPa (Liebske and Frost, 2012; de Koker et al., 2013). However, at higher pressures the measured eutectic melting curves are systematically lower in temperature than curves extrapolated on the basis of thermodynamic modelling of low-pressure experimental data, and those calculated from atomistic simulations. We find that our data are inconsistent with previously computed melting temperatures and melt thermodynamic properties of the $SiO_2$ endmember, and indicate a maximum in short-range ordering in $MgO$-$SiO_2$ melts close to $Mg_2SiO_4$ composition. The curvature of the model peridotite eutectic relative to an $MgSiO_3$ melt adiabat indicates that crystallization in a global magma ocean would begin at ~100 GPa rather than at the bottom of the mantle, allowing for an early basal melt layer. The model peridotite melting curve lies ~500 K above the mantle geotherm at the core-mantle boundary, indicating that it will not be molten unless the addition of other components reduces the solidus sufficiently. The model basalt melting curve intersects the geotherm at the base of the mantle, and partial melting of subducted oceanic crust is expected.

## 1. Introduction

Seismic velocity and density profiles of Earth's lower mantle as depicted in 1-D radially averaged models (Dziewonski and Anderson, 1981) are generally consistent with a peridotitic bulk composition. However, the exact proportions of the primary mineral phases, bridgmanite, ferropericlase, Ca-perovskite and possibly stishovite, are not yet uniquely constrained, and it is not known if the upper and lower mantle are compositionally similar, or if the lower mantle composition has a higher Si/Mg ratio due to a more chondritic primitive composition (e.g. Murakami et al., 2012) or through accumulation of mafic material via subduction. Seismology also reveals the presence of both small (e.g. Helffrich, 2006) and large-scale velocity anomalies (e.g. Garnero and McNamara, 2008) in the lower mantle. Large-scale features include two antipodal large low shear wave velocity provinces (LLSVP), as well as the more localized ultra-low velocity zones (ULVZ; Garnero and McNamara, 2008, Lay et al., 2008) just above the core-mantle boundary (CMB). Depending on their origin and mineralogical constitution, these structures may exert a strong control on the distribution and magnitude of heat flow at the CMB and, therefore, on the convective dynamics and evolution of the Earth (e.g. Nakagawa and Tackley, 2008; Torsvik et al., 2016).

One possible explanation for large-scale features in the deep lower mantle is mineralogical layering inherited from solidification of a deep global magma ocean during the earliest part of the Hadean Eon. Although geochemical arguments strongly preclude large-scale fractionation, segregation of bridgmanite-rich domains constituting up to ~15% of the lower mantle remain plausible (e.g. Walter et al., 2004; Liebske et al., 2005). Another possible mechanism is the continued accretion of subducted oceanic crust at the base of the mantle, and the potential for melting of that material at the CMB (e.g. McNamara and Zhong, 2005). Testing these possibilities requires a detailed knowledge of the melting behaviour of mantle materials at the extreme conditions of the lower mantle.

77      Recent experiments on natural peridotitic and basaltic compositions (Fiquet et

78      al., 2010; Andrault et al., 2011; Nomura et al., 2014; Andrault et al., 2014; Pradhan et al.,

79      2015) yield a range of solidus and liquidus temperatures at lower mantle pressures, and

80      it is difficult to discriminate between the effects of bulk composition, the presence or

81      absence of volatiles in starting materials, and the different melting criteria and detection

82      techniques used to establish the melting curves. In this study, we focus on eutectic

83      melting in the system MgO-SiO$_2$ in order to eliminate the complexity inherent in natural

84      multi-component systems. The MgO-SiO$_2$ system describes ~95% of the mineralogy of

85      peridotite and ~70% of basalt at lower mantle conditions. Importantly, because melting

86      is eutectic, compositions can be chosen that produce large amounts of melt at an

87      invariant melting temperature, facilitating greatly our ability to detect melting in

88      experiments at extreme pressures and temperatures.

89      **1.1 Previous Work in the System MgO-SiO$_2$ at Lower Mantle Pressures**

90      Eutectic melting in the MgO-MgSiO$_3$ binary has been studied experimentally

91      using the multi-anvil apparatus up to pressures of 26 GPa (Gasparik, 1990; Presnall et

92      al., 1997; Liebske and Frost, 2012). There is good agreement between these studies that

93      the bridgmanite + periclase = melt eutectic is located at ~2775 K at 25 GPa, and that the

94      eutectic liquid becomes progressively enriched in MgO with increasing pressure.

95      Liebske and Frost (2012) presented a thermodynamic model for eutectic melting in this

96      system, and based on extrapolation predicted that the eutectic liquid composition

97      becomes richer in MgO up to about 80 GPa (from ~57 mol% at 24 GPa to ~60 mol% at

98      80 GPa), at which point it maintains a nearly constant Mg/Si ratio that is close to model

99      bulk silicate earth (BSE). Atomistic simulations in the MgO-SiO$_2$ system by de Koker et

100     al. (2013) show a similar increase in MgO content from 58 to 60 mol% for the

101     bridgmanite + periclase eutectic liquid throughout the lower mantle pressure range (25

102     – 135 GPa). These authors also simulated melting in the MgSiO$_3$-SiO$_2$ binary, and found a

103 reduction in the MgO content of the bridgmanite + stishovite eutectic liquid from 37 to

104 33 mol% over the same pressure range; the silica phase is either stishovite or modified

105 stishovite in the CaCl$_2$ crystal structure (referred to as stishovite from here onwards).

106 No previous experimental studies have investigated eutectic melting in the MgO-

107 SiO$_2$ system throughout the lower mantle pressure range. The melting curves of the

108 unary compounds MgO, MgSiO$_3$ and SiO$_2$ have been investigated in the laser-heated

109 diamond anvil cell (LH-DAC) at pressures between ~30 and 60 GPa (e.g. Shen and Lazor,

110 1995), and results from these studies are in broad agreement with corresponding

111 melting curves calculated from atomistic simulations (Stixrude and Karki, 2005; de

112 Koker and Stixrude, 2009; de Koker et al., 2013). The experimentally derived melting

113 curve of bridgmanite (Zerr and Boehler, 1993 and Shen and Lazor, 1995), however,

114 maintains a considerably higher dT/dP slope and less curvature than the

115 computationally derived curve (de Koker and Stixrude, 2009 and Di Paola and Brodholt,

116 2016) through the 24-60 GPa pressure range.

117 In this study we performed double-sided laser-heated diamond-anvil cell

118 experiments to constrain eutectic melting temperatures in the MgO-SiO$_2$ binary system

119 up to 110 GPa. The two eutectics in the MgO-SiO$_2$ system are considered model

120 analogues for the melting of the natural lower mantle candidate lithologies, peridotite

121 and basalt, respectively.

122 **2. Experimental and Analytical Methods**

123 **2.1 Starting Compositions**

124 The compositions of the starting materials used in this study are listed in **Table**

125 **1**. In selecting starting compositions we aimed to be close to the eutectic melt

126 composition in both the MgO-MgSiO$_3$ and MgSiO$_3$-SiO$_2$ binary systems, as predicted in

127 the studies of Liebske and Frost (2012) and de Koker et al (2013). In the MgO-MgSiO$_3$

system we chose a composition with 58 mol% MgO, whereas in the MgSiO$_3$-SiO$_2$ system

we chose two mixes, one with 40 mol% MgO and the other with 35 mol% MgO.

**Table 1.** Experimental starting compositions (in mol%)

| Starting mixtures | SiO$_2$ | MgO | Components* |
|---|---|---|---|
| M$_{58}$S$_{42}$ | 42 | 58 | En + Fo |
| M$_{40}$S$_{60}$ | 60 | 40 | En + SiO$_2$ |
| M$_{35}$S$_{65}$ | 65 | 35 | En + SiO$_2$ |

*En: enstatite glass (MgSiO$_3$), Fo: crystalline forsterite (Mg$_2$SiO$_4$), SiO$_2$: silica glass

**Fig. 1** shows our starting compositions relative to the predicted eutectic

compositions derived from the atomistic computations of de Koker et al. (2013), and by

applying the lever rule we calculate that our near-eutectic starting materials should

yield from ~50% to 95% melt at lower mantle pressures. Producing such a large liquid

fraction upon melting aids considerably in melt detection during laser heating and

therefore enables higher precision on eutectic temperature assessment.

The MgO-MgSiO$_3$ binary composition was made by mixing enstatite glass with

crystalline forsterite in the desired proportions, followed by grinding in an agate mortar

under ethanol to a powder with a grain size of ~1 μm. Enstatite glass was made from a

1:1 molar mix of pure MgO and SiO$_2$ oxides, which were fused three times at 1 atm and

~1700 °C for 30 minutes. The pure, crystal free glass product was ground after each

fusion to a very fine powder. Crystalline forsterite was synthesized from a 2:1 molar mix

of pure MgO and SiO$_2$ oxides, which were sintered three times at 1 atm and 1500 °C for

one hour and was verified as a pure phase by X-ray diffraction. The MgSiO$_3$-SiO$_2$ binary

compositions were made by mixing enstatite glass (prepared as above) and high purity

optical-grade silica glass (99.997%) in the desired proportions followed by grinding in

an agate mortar under ethanol to a powder with a grain size of ~1 μm. Before weighing,

all powdered components were dried at 120 °C and stored in a desiccator to prevent

adsorption of water. To provide an absorber for the IR laser radiation, ~10 wt% of sub-

micron tungsten powder was added to each starting composition. These mixtures were

150     then further ground in an agate mortar under ethanol to ensure that the W absorber

151     was homogeneously distributed throughout the sample on the micron scale to provide

152     as uniform heating as possible. All mixtures were stored at 120 °C under vacuum before

153     use.
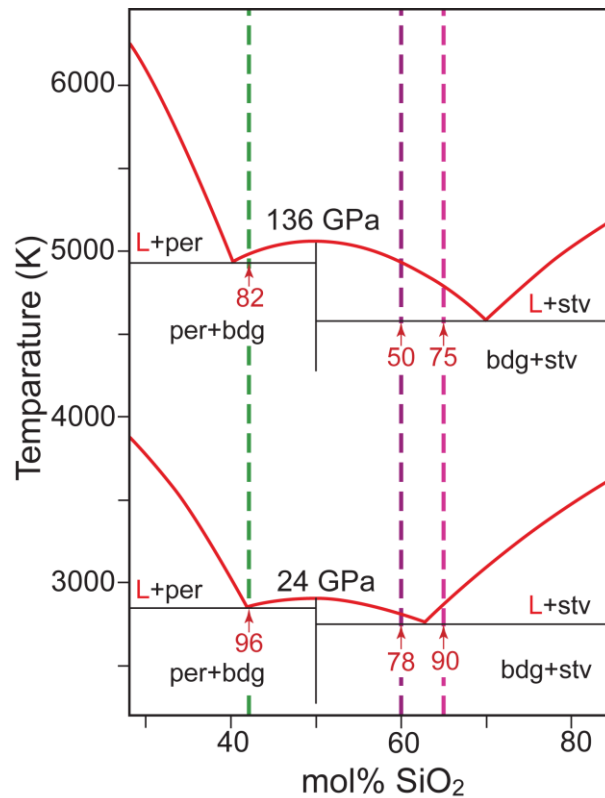


154

155     **Fig. 1.** Liquidus phase relations in the MgO-SiO$_2$ system at 24 and 136 GPa, adopted from

156     de Koker et al. (2013). The initial fractions of eutectic melt (in percent) for the bulk

157     starting compositions at 42, 60 and 65 mol% silica are calculated by the lever rule and

158     shown beneath the red arrows representing the three starting compositions. Bdg =

159     bridgmanite, per = periclase, stv = stishovite and L = liquid.

160

161     **2.2 LH-DAC Experiments**

162     **2.2.1 High Pressure generation**

163    High-pressure experiments were performed in 'Princeton-type' symmetric DACs,

164    using Type Ia diamond anvils with culet diameters of 120, 150, 200 or 250 μm. Re

165    gaskets were pre-indented to ~30 GPa and sample chambers were drilled by UV laser

166    ablation in each indentation.  We drilled multiple sample chambers in a single Re-gasket

167    where space allowed; 3 holes when using 200 μm diameter culets for pressures of 60-90

168    GPa, and 4 holes when using 250 μm diameter culets for pressures of 24-60 GPa (Walter

169    et al., 2015; Thomson et al., 2014).  The initial sample chamber diameters were 25-30

170    μm, and all sample chambers drilled in one gasket were filled with the same starting

171    material. Before sealing and pressurising, the loaded DAC was heated at 125 °C under Ar

172    gas flow for at least one hour to remove adsorbed water and then closed at the same

173    high temperature conditions.

174    We opted not to use an additional thermally insulating material between the

175    sample and the diamond anvils in order to avoid chemical reactions and mechanical

176    effects at high pressures (e.g. sample tearing and separation) that might affect the

177    observed melting temperatures. This is especially important as we have designed the

178    bulk compositions to produce high melt fractions at the invariant temperature to aid in

179    melt detection.

180    **2.2.2 Pressure Measurement**

181    Pressure was determined on the basis of the Raman shift of the singlet peak

182    related to stress in the (001) direction at the diamond culet surface (Hanfland et al.,

183    1986), and is calibrated relative to the ruby fluorescence scale of Mao et al (1986) (see

184    Walter et al., 2015).  Confocal Raman measurements were made using a Jobin-Yvon

185    T64000 Raman microscope at a spectral resolution of ~0.4 cm$^{-1}$ within a diffraction

186    limited focal volume. The calibrations based on diamond peak-shift are shown in **Figure**

187    **S1** in the supplementary information. In each experiment, pressure was directly

188    measured on each sample chamber before and after laser-heating. All reported

189 pressures in this study are post-heating measurements. No correction has been made

190 for thermal pressure during heating due to lack of *in situ* EoS data. The thermal effect on

191 pressure is not expected to be more than ~10% of the initial pressure measured at room

192 temperature (Fiquet et al., 2010 and Andrault et al., 2011). None of the results reported

193 here came from heating of the sample chambers that contained ruby as it was added

194 only for the purpose of pressure calibration.

195

196 **2.2.3 Laser Heating**

197 Double-sided laser heating was performed at the University of Bristol using two

198 100 W Yb-doped fiber lasers ($\lambda$=1070 nm) combined with beam-shaping and beam-

199 expanding optics to minimise radial temperature gradients. Beams were shaped to an

200 approximately 'flat-top' energy distribution, with the spot size matched as closely as

201 possible to the diameter of the sample chamber. The melting experiments were heated

202 using an automated 'ramp mode', in which the laser power is continually and

203 automatically increased by ~0.2 watts on each side every 4-6 seconds until quenching,

204 resulting in a heating rate of 500-1500 K/min. We also performed a series of subsolidus

205 experiments, where samples were heated to target temperatures below our melting

206 curve and maintained at that temperature for ~30 minutes before quenching.

207 **2.2.4 Temperature Measurement**

208 At each step, temperatures were measured using standard spectroradiometric

209 techniques (e.g. Walter and Koga, 2004). The thermal emission spectra were measured

210 on both sides of the sample simultaneously over a wavelength range of 570 - 830 nm

211 along an approximately 2 μm wide strip across the sample. Spectral intensity profiles

212 were converted to temperatures by normalising to a NIST calibrated W-lamp of spectral

213 radiance, with spectra fitted to the idealised grey-body Wien function. Maximum

214  temperature precision is achieved by selecting the best-fit 200 nm bandpass within the

215  570 - 830 nm window that minimizes the average analytical error on the fits;

216  temperature precision is typically better than 10 K at 3000 K. Uncertainty in

217  temperature accuracy related to possible wavelength dependent sample emissivity (e.g.

218  non-grey body behaviour) is unknown. A boxcar smoothing procedure was performed

219  on all temperature profiles to eliminate artefacts that arise because the spatial

220  resolution of the CCD at the object plane (~1 μm) is smaller than the actual system

221  optical resolution of ~3 μm. For more details on the laser heating and temperature

222  measurement system employed here, including calibration, benchmarking and

223  uncertainties, see Lord et al. (2014a).

224      In several experiments we also obtained 2D temperature maps using four-color

225  imaging radiometry similar to that described in Campbell (2008). In brief, a 50x image

226  of the sample is focussed onto a large format, high resolution CCD (SBIG Model ST-

227  402ME) at four different wavelengths (550, 650, 750 and 850 nm). The images are

228  superimposed in software to a precision of ± 1 pixel. Temperature is calculated from a

229  four-color Wien fit at each pixel, with spectral intensity calibrated as described above

230  for the 1D spectroradiometry system.

231  **2.3 Analytical Methods**

232      After decompression, the culet region of the gaskets were cut out by UV laser

233  ablation, transferred to a 1-inch epoxy mould and embedded in standard epoxy. The

234  cured epoxy discs were polished axially to expose the approximate centre of the sample

235  chambers, first manually using water based 9 μm diamond suspension on a polishing

236  cloth, and later using a Buehler EcoMet® grinder-polisher with 3 μm and 1 μm diamond

237  suspension. Because the samples were very thin (~10 – 25 μm) and usually not

238  completely flat after decompression, approximately 50% of all the sample chambers

239  were lost during this process. Successfully polished samples were coated with a thin

240 layer of carbon or gold and analysed using a JEOL JXA8530F Field Emission Gun Electron

241 Microprobe at the University of Bristol. Textural and chemical analyses were carried out

242 with beam conditions of 5 keV and 20 nA. Wave-length dispersive elemental calibration

243 was performed with the following standards: Si - synthetic $SiO_2$ crystal, Mg – synthetic

244 MgO crystal, Al - Amelia albite and W - tungsten metal.

245 **3. Results**

246 **3.1 Melt Detection: Thermal Signal Processing**

247 Perturbations in the temperature-power relation as laser power increases have

248 been shown to be an extremely robust indicator of melting. These perturbations

249 commonly manifest as a distinct plateau in temperature as laser power increases;

250 temperature plateaus are especially well defined during invariant melting of metals, but

251 have also been used to effectively detect melting in low-variance silicate, silicate-

252 carbonate, and silicate-water systems (e.g. Shen and Lazor, 1995; Anzellini et al., 2013;

253 Lord et al., 2014a; Thomson et al., 2014; Walter et al., 2015). A comprehensive

254 understanding of the factors resulting in thermal signal perturbations related to phase

255 changes is elusive due to the diabatic nature of the sample environment and a lack of

256 knowledge of material specific factors including changes in optical, thermal and

257 mechanical properties upon crystallisation and/or melting (see for example: Geballe and

258 Jeanloz, 2012; Lord et al., 2014a,b). Critically, this method has been corroborated using

259 independent techniques, including direct observation of melt by *in situ* X-ray diffraction,

260 often simultaneously (e.g. Anzellini et al. 2013; Lord et al. 2014a,b).

261 In all automatically ramped experiments, temperature was measured

262 continuously at ~5s intervals during the heating ramp. We observe in some cases the

263 appearance of a well-defined plateau in temperature as power continues to increase

264 (**Fig. 2a-c**), but also commonly observe a rapid rise in temperature to a distinct

265 temperature maximum that occurs after a gradual rise in temperature (**Fig. 2d-f**). These

266 perturbations are likely a consequence of the indirect heating of the silicate due to laser

267 absorption by the dispersed W particles and mechanical segregation of a high-degree

268 melt and W particles. We observe the temperature maxima at these perturbations to be

269 pressure dependent, and we correlate these with eutectic melting of the sample.

270 Textural observations support this interpretation.
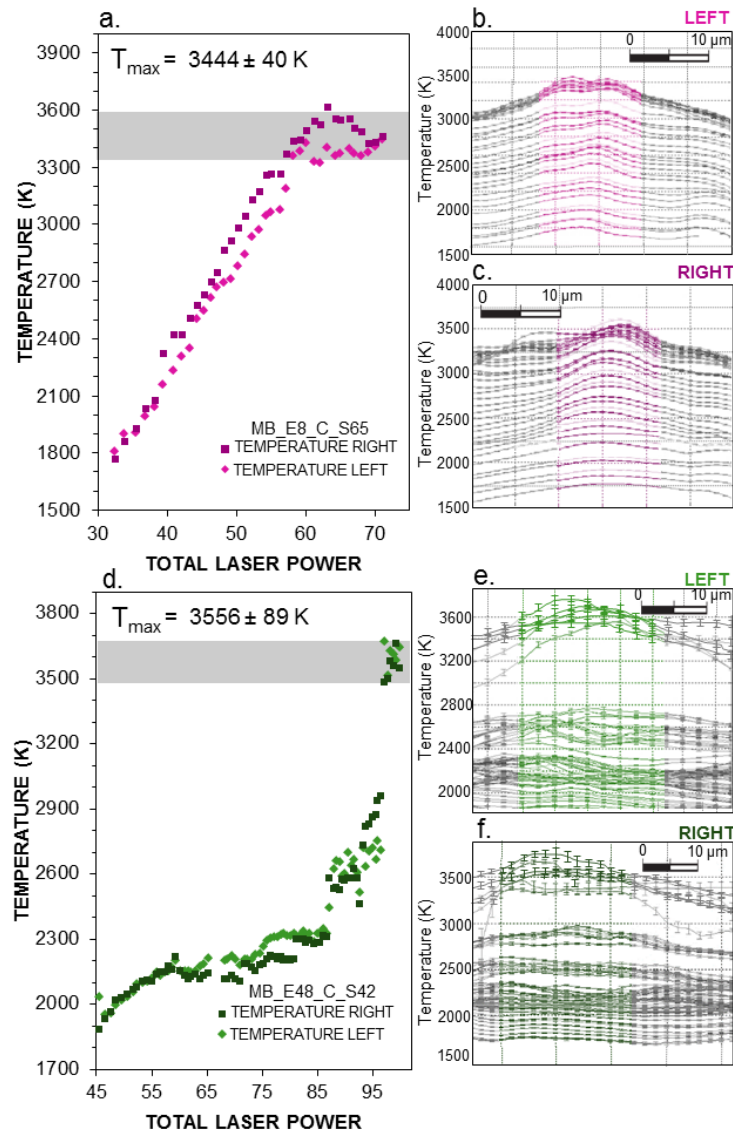
271



272 **Fig. 2.** Example of automatically ramped melting experiments showing: **(a)** Peak

273 temperatures measured on the right (purple squares) and left (pink diamonds) sides of

274 the DAC vs. total laser power in experiment MB_E8_C, and showing a well-developed

275 temperature plateau. The pale grey band represents a 1 σ uncertainty in the mean of the

276 points within the plateau (defined by the grey band); **(b, c)** temperature profiles across

277 the heated spot recorded on both sides of the DAC for experiment MB_E8_C. The ranges

278 highlighted in colour reflect the selected windows used to define peak temperature. The
279 sample chamber size is approximately 30 μm and the selected window is about 15 μm.
280 Error bars reflect the precision of the Wien fits and are ±1σ; **(d)** Peak temperatures vs.
281 laser power for experiment MB_E48_C showing a rapid increase in temperature before
282 reaching a maximum temperature plateau; **(e, f)** temperature profiles across the heated
283 spot for MB_E48_C.

284 **3.2 Melting Detection: Textural Analysis**

285     Textural and compositional analysis of recovered samples using backscattered

286 electron imaging (BSE) and elemental mapping provide additional evidence for melting.

287 To establish the baseline subsolidus texture, experiments were made well below the

288 expected melting temperatures and at conditions approaching the solidus (**Tables S1**

289 and **S2** in supplementary materials).  All subsolidus samples we inspected using BSE

290 imaging showed a relatively uniform distribution of W particles embedded in the silicate

291 matrix, with no obvious indication of melting in the heated area (**Fig. 3a,b**). However,

292 we do observe a distinct coarsening of the W grains at higher temperatures approaching

293 the solidus (**Fig. 3b)**. In sharp contrast, samples where melting was detected by thermal

294 signal processing show a range of textures consistent with melting, typical examples of

295 which are shown in **Fig 3c**. The samples show segregation of W grains into a ring, or in a

296 radial geometry about a central region that is relatively W-free. We also commonly

297 observed a more centrally located large W aggregate (**Fig. 3c)**. We suggest that once a

298 large melt fraction forms at the eutectic temperature, W grains are mechanically

299 displaced by the melt, resulting in the observed segregation of silicate melt pool and W

300 aggregates. Melt-W segregation may also provide at least a partial explanation for the

301 increased power needed to maintain constant temperature at the eutectic.
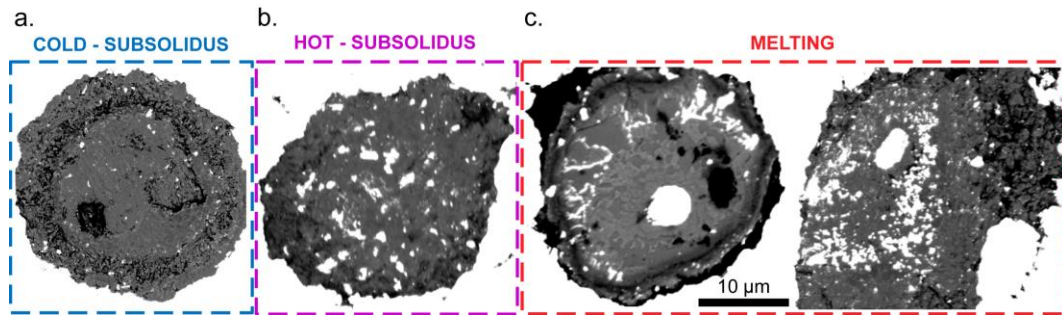
**Fig. 3.** BSE images of recovered DAC samples from: **(a)** cold-subsolidus (MB_E44_B P = 53.3 GPa and $T_{max,s}$ = 2350 K), **(b)** hot-subsolidus (MB_E36_C P = 36.7 GPa and $T_{max,s}$ = 2500 K), and **(c)** melted experiments (left: MB_E11_B P = 43.7 GPa and $T_m$ = 2930±124 K, right: MB_E3_C P = 28.6 GPa and $T_m$ = 2753±35 K).

The formation of a central aggregate and radially distributed W could indicate melting of the W absorber. However, we are confident that our melting curves represent the melting of the silicate rather than the W absorber because the 1 atm melting point of W (3687 K; Handbook of Physics and Chemistry) is considerably higher than most of our melting data. Another possibility is melting of the absorber as a consequence of carbide formation by reaction with the diamond. This is also an unlikely explanation as we observe no carbide formation in our electron probe analyses (W grains and/or aggregates are made of pure W), and the diamond anvil culet surfaces show no indications of reaction with the sample. Moreover, the melting point of tungsten carbide at 1 atm (3003–3103 K, Sittig's Handbook of Toxic and Hazardous Chemicals and Carcinogens) is higher than most of our data points below 40 GPa for the MgO-rich eutectic and 60 GPa for the $SiO_2$-rich eutectic, and as we will show below, our melting data at the lowest pressures investigated are consistent with results from multi-anvil apparatus experiments and *ab initio* simulations.

### 3.3 Melt Detection: Chemical Analysis

Polished samples were analysed with the electron probe to generate high-resolution X-ray elemental maps for Si, Mg and W, as well as spot chemical analyses. **Fig. 4** shows an example using the $M_{35}S_{65}$ starting material, where samples were pressurized

325 to almost identical pressure (~50 GPa) but heated to different temperatures. **Fig. 4a**

326 shows a sample heated to 2000 K for 35 minutes, and **Fig. 4b** represents a sample

327 heated to 2300 K for several minutes. Both samples show a relatively uniform

328 distribution of W, indicating the samples remained subsolidus.
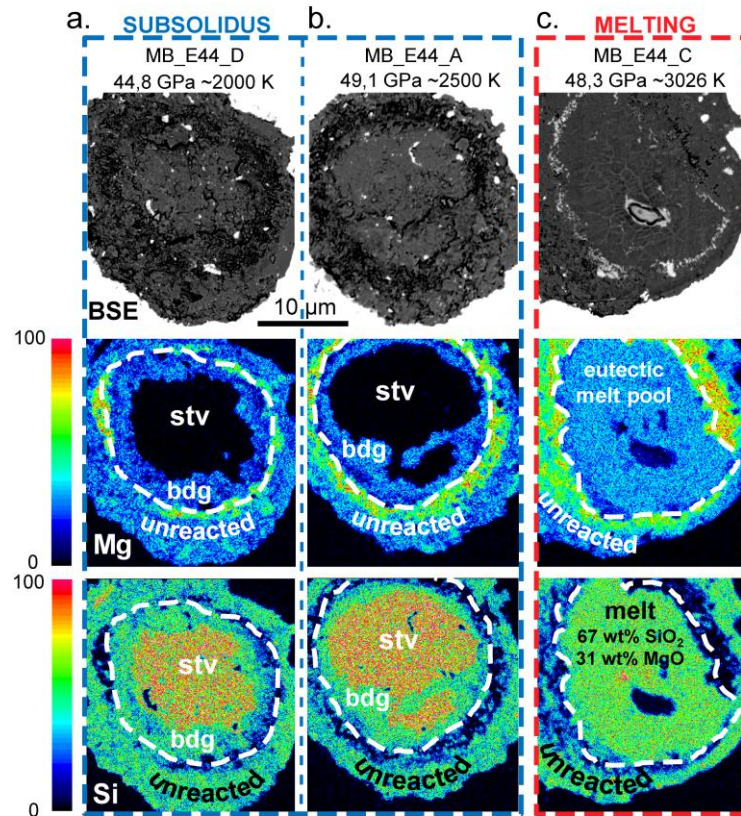
329



330 **Fig. 4.** Backscattered electron images (BSE) and wavelength dispersive elemental maps

331 for Mg and Si of run products in the $MgSiO_3$-$SiO_2$ sub-system. **(a,b)** Two subsolidus

332 samples (MB_E44_D and A) showing a homogeneous distribution of W grains in the BSE

333 images, and phase segregation between bridgmanite (bdg) and stishovite (stv) in the

334 heated region. **(c)** The melted sample (MB_E44_C) shows the typical annulus of W grains

335 and a central aggregate in BSE, whereas the heated region shows a single homogeneous

336 silicate with a composition close to that of the starting eutectic composition (67 wt%

337 $SiO_2$ and 31 wt% of MgO), which we interpret as quenched melt

338 The Si- and Mg-chemical maps and spot analyses indicate the presence of two

339 phases in the heated region, one of pure $SiO_2$, which we interpret as stishovite, and one

340 with an intermediate Mg/Si ratio consistent with bridgmanite (the grains were too small

341    <500 nm for individual mineral analyses). The sample shown in **Fig. 4c** (MB_E44_C) was

342    heated in ramp mode with melting detected by thermal signal processing at 3026 ±178

343    K at 48,3 GPa. Here again, we observe the typical W-ring around the quenched melt pool

344    and also a W-aggregate in the middle. The Si- and Mg-elemental maps show a large,

345    chemically homogeneous central area with an Mg/Si ratio intermediate between

346    bridgmanite and stishovite, indicative of a quenched eutectic melt. We performed

347    chemical mapping like that shown in **Fig. 4** on a number of samples in both the MgO-

348    $MgSiO_3$ and $MgSiO_3$-$SiO_2$ systems, with similar and consistent results. The textural and

349    chemical analyses fully support the interpretation from thermal signal processing of

350    sample melting.

351    The subsolidus chemical maps (**Fig. 4a,b**) show phase separation between

352    bridgmanite and stishovite , which is likely due to Soret or saturation gradient diffusion

353    in response to the temperature gradient through the sample (e.g. Sinmyo and Hirose,

354    2010). We observe $SiO_2$ crystallizing within the hottest region, with bridgmanite

355    intergrown or forming an annulus around stishovite, consistent with $SiO_2$ diffusing to

356    the hot region. Temperature gradient induced phase segregation is also common in

357    multi-anvil experiments where the temperature gradients are much less extreme (e.g.

358    100 C/mm), and have been reported previously to occur in the MgO-$SiO_2$ system

359    (Presnall and Walter, 1993).

360    **3.4 2D - Sample Temperature Distribution**

361    The radial temperature distribution, as measured by 2-D imaging radiometry,

362    varies in detail from sample to sample but has common features. **Fig. 6** shows two

363    examples, one showing a subsolidus temperature distribution (**Fig. 5a**), and another

364    showing the temperature distribution after a temperature-power perturbation

365    interpreted as melting (**Fig. 5b**). In the subsolidus we commonly observe a ~15 μm

366    diameter region with roughly constant temperature (~±50 K), surrounded by a region

367 where temperature decreases with increasing distance from the centre at ~20-30 K/μm,

368 mimicking the energy distribution of the incident laser radiation. This gradient

369 continues up to the radius at which the intensity of the incandescent light drops to

370 ~10% of the maximum and an accurate temperature fitting becomes impossible (the

371 dark blue region in **Fig. 5**). This masks the steep gradient of ~$10^3$ K/μm that defines the

372 edge of the laser heated region. Such a temperature distribution is stable for extended

373 duration (e.g. tens of minutes). However, with continuous increase in laser power and

374 temperature, we observe a drastic, time-dependent change in temperature distribution

375 (e.g. **Fig. 5b**) that correlates with the melting perturbation (plateau). **Fig. 5b** shows a

376 central temperature peak and an annulus of high temperatures separated by a slightly

377 cooler zone that mimics closely the distribution of W typically observed upon melting of

378 the sample (**Fig. 3 and 4**).
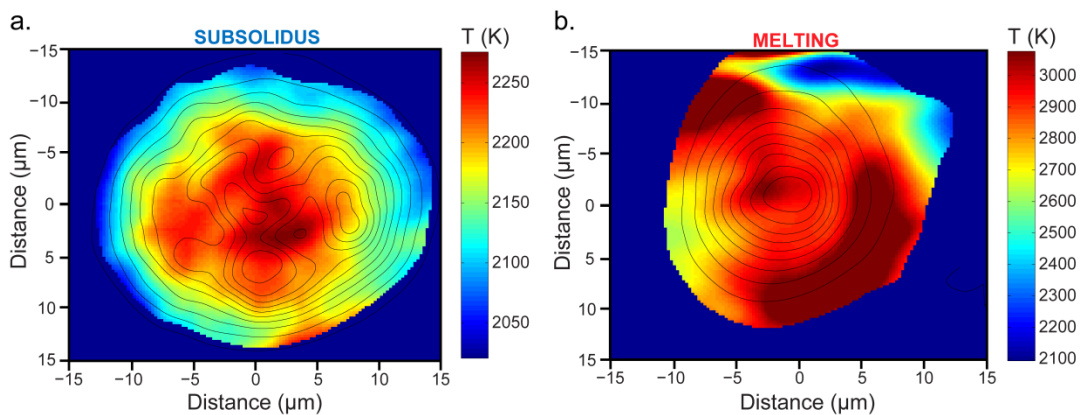
379



380 **Fig. 5.** 2-D temperature maps over the laser-heated region in LH-DAC experiment
381 MB_48_C at 48.3 GPa as determined using 4-color imaging radiometry. **(a)** Subsolidus
382 temperature map collected at the beginning of laser-heating at ~2300 K. **(b)** Super-
383 solidus temperature map collected just before quenching at ~3000 K. Contour lines
384 represents light intensity relative to the maximum at intervals of 10%. The dark blue
385 regions are not fitted because of insufficient light intensity that coincides with the very
386 steep temperature gradient (~$10^3$ K/μm) separating the laser heated region from its
387 unheated surrounding. See text for more details.

388    An axial temperature gradient must also be present between the diamond anvils

389    over a thickness of ~10–25 µm (depending on pressure), but is not well defined because

390    we cannot measure it directly. We expect an ~5 – 10 µm region in the centre across

391    which temperature decreases at the modest rate (~±50 K/µm), and a steep gradient

392    over a few microns toward the highly thermally conductive diamond surfaces on each

393    side.

394

395    **3.5 Melting Curves**

396    The melting temperatures reported in this study are calculated as the mean of

397    the smoothed maximum temperatures ($T_{max,s}$ data in **Table S1** and **S2 in**

398    **supplementary materials**) from both sides of the sample, from the start of the

399    temperature plateau until quenching. The reported uncertainties include the analytical

400    precision in the greybody spectral fitting and one standard deviation of the temperature

401    variation within the melting plateau, which results in total uncertainties of ~50 – 300 K.

402    We do not include an uncertainty related to non-greybody sample emissivity. Similarly,

403    in subsolidus experiments we report temperatures calculated as the mean of the

404    measured maximum temperatures on both sides of the sample, starting from the power

405    at which the target temperature was reached until quenching. The run conditions of

406    melting and subsolidus experiments are listed in **Tables S1** and **S2** in the

407    supplementary materials and the results are plotted in **Fig. 6**.
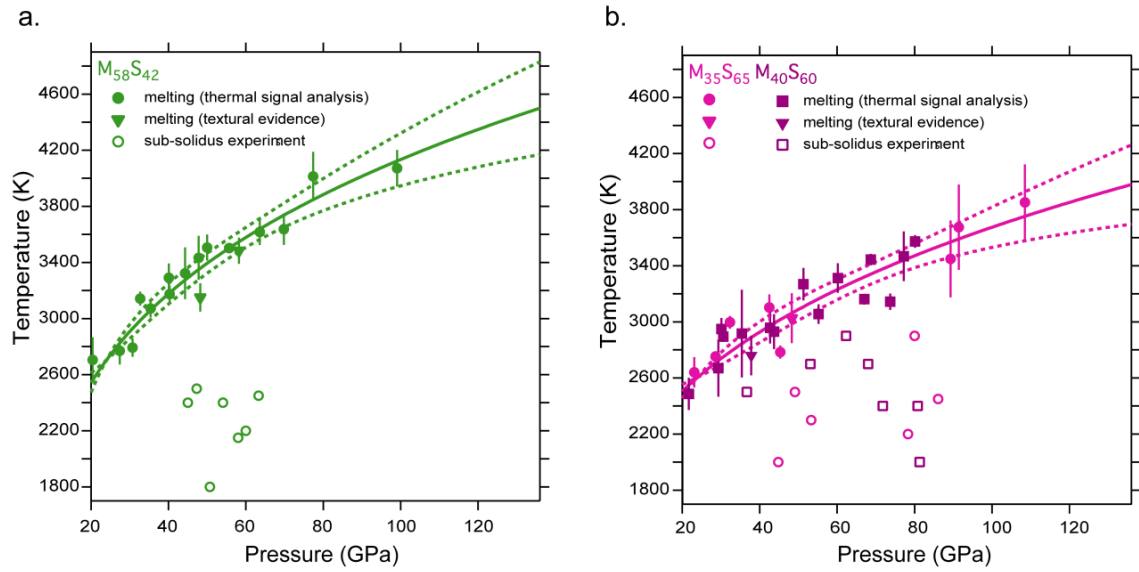
**Fig. 6.** Results of this study for **(a)** the MgO-MgSiO$_3$ eutectic (M$_{58}$S$_{42}$), and **(b)** the MgSiO$_3$–SiO$_2$ eutectic (M$_{35}$S$_{65}$ and M$_{40}$S$_{60}$). The melting curves (solid lines) are fitted using a modified Simon-Glatzel equation (Simon and Glatzel, 1929) with parameters listed in **Table S3** and extrapolated to 136 GPa with associated 95% confidence intervals (dashed lines).

All ramped experiments that resulted in detectable melting plateaus were used to constrain the melting curves. We could not detect any statistical difference between the melting data for the two Si-rich compositions we studied in the MgSiO$_3$-SiO$_2$ system, as expected for a eutectic system. Therefore, we fitted all the data simultaneously to produce a single eutectic melting curve. The P-T data are fitted using a modified Simon-Glatzel equation:

$$T_m = T_{24} \left( 1 + \frac{P_m}{A} \right)^{\frac{1}{C}} \tag{1}$$

where $T_m$ is the melting temperature at pressure $P_m$, $A$ and $C$ are fitting parameters (see **Table S3** in supplementary materials), and $T_{24}$ is the melting temperature at 24 GPa from this study, which is consistent with both Liebske and Frost (2012) and de Koker et al. (2013). Because the lower mantle mineral assemblages differ from those at ambient pressure conditions, we use $T_{24}$ as the starting point for our fits rather than the commonly used $T_0$ in the original Simon-Glatzel equation (Simon and Glatzel, 1929). The

19

426  reference melting temperature at 24 GPa ($T_{24}$) represents approximately the pressure at

427  which bridgmanite becomes stable. The melting temperatures for the two eutectics can

428  be fitted with curves with positive and decreasing dT/dP slopes through the lower

429  mantle pressure range.

430  **4. Discussion**

431  **4.1 Comparison with Previous Work in the MgO-SiO$_2$ System**

432  In **Fig. 7** we compare our experimentally determined eutectic melting curves

433  with previously published results from atomistic simulations (de Koker et al., 2013),

434  previous experiments, thermodynamic modelling (Liebske and Frost, 2012), and

435  endmember melting temperatures for MgSiO$_3$ (Stixrude et al. 2009), SiO$_2$ (Shen and

436  Lazor, 1995) and MgO (Alfé, 2005). Our MgO-MgSiO$_3$ eutectic melting curve is in

437  excellent agreement with the experimental data of Liebske and Frost (2012) in the

438  lower pressure range (24 – 26 GPa). However, at higher pressures our melting curve is

439  systematically lower than their extrapolated melting curve predicted on the basis of

440  thermodynamic modelling. The predicted melting curve of Liebske and Frost (2012) is a

441  maximum of ~350 K higher than our curve; at the pressure of the core-mantle boundary

442  it lies within our uncertainty envelope. The bridgmanite + periclase eutectic as

443  calculated by de Koker et al. (2013) is higher than our curve by about 100 K at 24 GPa,

444  and about 450 K at 136 GPa.

445  The liquidus diagram for the MgSiO$_3$-SiO$_2$ system at lower mantle pressures has

446  not been previously studied experimentally. The first principles calculations of de Koker

447  et al. (2013) in this system predict eutectic melting temperatures of about 2740 K and

448  4580 K at 24 and 136 GPa, respectively, which are about 230 K and 600 K above our

449  melting curve at these pressures.

450
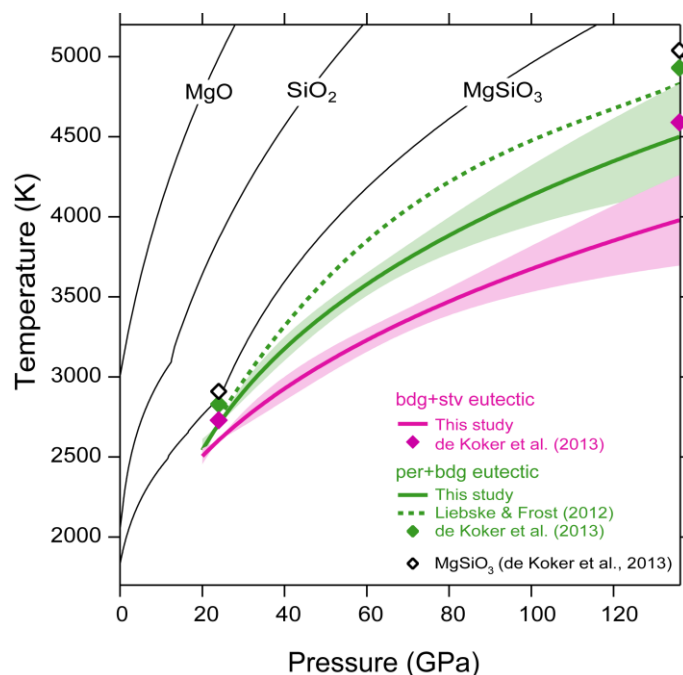
**Fig. 7.** Eutectic melting curves from this study (solid lines with shaded area) compared with results from atomistic calculations (solid diamonds - de Koker et al., 2013), thermodynamic modelling (dashed line - Liebske & Frost, 2012) and melting curves of endmembers $MgSiO_3$ (Stixrude et al. 2009), $SiO_2$ (Shen and Lazor, 1995) and MgO (Alfé, 2005). The green and pink melting curves represent the peridotitic ($M_{58}S_{42}$) and basaltic ($M_{35}S_{65}$ and $M_{30}S_{60}$) model eutectics, respectively. The model basalt melting curve has a lower dT/dP-slope and less curvature than the model peridotite melting curve throughout the lower mantle pressure range.

The systematically lower melting points in our work compared to the first principles calculations might be explained by the difficulty in obtaining accurate melting points ($T_m$) in polyatomic systems using *ab initio* molecular dynamics. Simulations of relatively small systems (66-78 atoms, de Koker et al., 2013) with periodic boundary conditions tend to overestimate $T_m$ due to the lack of defects and surfaces on which melt can nucleate.

**4.2 Comparison with Melting Curves of Natural Compositions**

**Fig. 8** compares our eutectic melting curves with experimentally determined solidi for natural basalts and peridotites. Eutectic melting curves in the $MgO$-$SiO_2$ binary

468   system should be higher than in systems that contain additional components. The multi-

469   component peridotite solidi of Fiquet et al. (2010), Andrault et al. (2014) and Nomura et

470   al. (2014) are shown in **Fig. 9a**. Fiquet et al. (2010) used a combination of X-ray

471   scattering and textural evidence to detect melting in a model upper mantle composition

472   (KLB-1), and found a solidus that is about 200 K lower than the bridgmanite + periclase

473   eutectic determined here, but with an almost identical curvature. Andrault et al. (2011),

474   also relying on X-ray diffraction and textural evidence for melt detection, found a solidus

475   for model chondritic peridotite that has little or no curvature and which is located below

476   the bridgmanite + periclase eutectic by a maximum of ~600 K at 80 GPa, but is within

477   300 K at the lower and higher pressure extremes. The pyrolitic peridotite solidus

478   determined by Nomura et al. (2014) also has small curvature, but is about 1000 K below

479   the bridgmanite + periclase eutectic at 80 GPa, and well below the other natural

480   peridotite melting curves. Our peridotite melting curve is higher than those of natural

481   compositions due to the reduction in temperature caused by the solution of additional

482   components into the melt, with iron likely to have the most significant effect. For

483   example, de Koker et al. (2013) suggest adding around 10 mol% Fe to the MS system

484   would reduce the solidus by 250±50 K. Such a reduction would bring our melting curves

485   into much closer agreement with those of Fiquet et al. (2010) and Andrault et al. (2011)

486   in the peridotitic system, though the curvature would still more closely resemble the

487   study of Fiquet.

488        The different melting temperatures observed among studies in multi-component

489   systems must reflect compositional differences to some degree (e.g. Mg/Si ratio, $H_2O$

490   content), but differences in melt detection criteria are also likely to be relevant. In

491   natural systems melting occurs over a temperature interval, rather than at a eutectic

492   temperature. The X-ray scattering techniques used in the studies of Fiquet et al. (2010)

493   and Andrault et al (2011) (e.g. diffuse scattering; grain growth; phase disappearance)

494   likely lead to overestimation of the solidus temperature because a substantial melt

495 fraction may need to be present before melt can be detected. Nomura et al. (2014)

496 attribute their lower temperature solidus to a combination of more sensitive melt

497 detection technique based on X-ray tomographic imaging, and to the presence of ~400

498 ppm $H_2O$ in their starting composition.

499 The multi-component basalt solidi of Hirose et al. (1999), Andrault et al. (2014)

500 and Pradhan et al (2015) are shown in **Fig. 8b**. Both Hirose et al. and Pradhan et al. use

501 thermal signal processing as a primary melting criterion, their melting curves are nearly

502 identical, and are supported at the low-pressure end by multi-anvil press (MAP)

503 experiments. The melting curves from these studies have a nearly identical shape to the

504 bridgmanite + stishovite eutectic curve found in our experiments, and lie close to our

505 melting curve. This would suggest that addition of iron and other components has little

506 effect on solidus temperature. However, in contrast, the basaltic solidus of Andrault et

507 al. (2014), determined using X-ray diffraction and temperature plateaus as melting

508 criteria, falls ~600 K below our bridgmanite + stishovite melting curve at 30 GPa, and

509 ~300 K below at pressures greater than about 60 GPa. As with peridotite melting, melt

510 detection in multi-component basaltic systems will depend on the melt fraction

511 exceeding the detection limit. For example, in the study of Hirose et al., the basalt sample

512 was 'sandwiched' between Re absorbers, and melting was detected by a rapid rise in

513 temperature. It may be that melting occurs at a lower temperature, and the runaway

514 heating occurs only after considerable melt is present such that the solidus temperature

515 is overestimated.

516 We reiterate that the advantage of working in the MgO-SiO₂ system using near-

517 eutectic starting compositions is that large amounts of melt are produced at a single

518 eutectic temperature, allowing a more accurate determination of melting. In contrast,

519 the melting curves produced in studies on natural compositions may represent the

520 temperature at which the melt fraction exceeds the detection limit of the method used

for melt determination, whether it be thermal signal processing or *in situ* X-ray

diffraction methods.



523
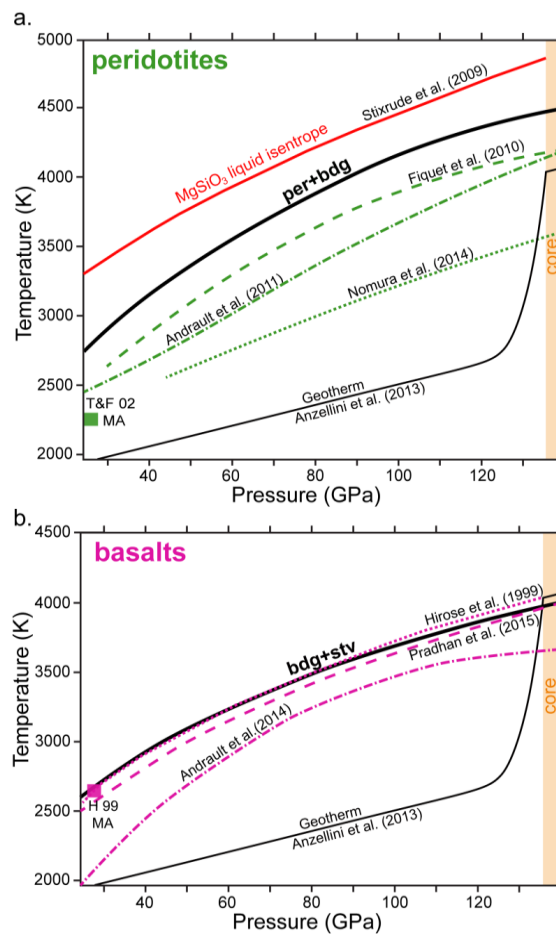
**Fig. 8.** A comparison of experimentally determined melting curves (thick black solid lines) in this study of: **(a)** the bridgmanite + periclaseeutectic compared with the peridotite solidi determined in LH-DAC experiments by Fiquet et al. (2010), Andrault et al. (2011), Nomura et al. (2014) and MAP experiments by: Trønnes and Frost (2002), together with the MgSiO$_3$ liquid isentrope from Stixrude et al. (2009); **(b)** the bridgmanite + stishovite eutectic compared with the basalt solidi determined in LH-DAC experiments by Hirose et al. (1999), Andrault et al. (2014) and Pradhan et al. (2015) together with a single MAP experiment from Hirose et al. (1999). The mantle adiabat of Anzellini et al. (2013, supplementary) is shown for comparison.

**4.3 Implications for Thermodynamic Modelling of the MgO-SiO$_2$ System**

The eutectic melting curves presented in this study provide constraints on the thermodynamic properties of the MgO-SiO$_2$ liquid solution. By employing *ab initio*

24

536    derived endmember models for the solids (periclase and stishovite) and liquids (MgO

537    and $SiO_2$) from de Koker et al. (2013) and references therein, we calculated the activities

538    ($a_i$) of MgO and $SiO_2$ in the two eutectic liquids using the equilibrium relation:

$$\mu_i = G_i^{\circ} + RT \ln a_i \tag{2}$$

539    where $G_i^{\circ}$ is the Gibbs free energy of component $i$ (e.g. MgO or $SiO_2$) in the pure

540    endmember melt and $\mu_i$ is the chemical potential of that component in the melt. At the

541    bridgmanite + periclase eutectic, the chemical potential of MgO liquid is equal to the

542    Gibbs free energy of periclase (assuming no $SiO_2$ is incorporated into periclase, Equation

543    2). The same is true of $SiO_2$ liquid and stishovite for the bridgmanite + stishovite eutectic

544    (Equation 3). The thermodynamic relationships can be described as:

$$\mu_{MgO}^{liquid} = \mu_{MgO}^{solid} \tag{3}$$

$$\mu_{MgO}^{\circ,liquid} + RT \ln a_{MgO} = \mu_{MgO}^{\circ,solid} \tag{4}$$

545    and

$$\mu_{SiO_2}^{liquid} = \mu_{SiO_2}^{solid} \tag{5}$$

$$\mu_{SiO_2}^{\circ,liquid} + RT \ln a_{SiO_2} = \mu_{SiO_2}^{\circ,solid}. \tag{6}$$

546    As the resulting activities only rely on endmember properties, they can be used to assess

547    the accuracy of MgO-$SiO_2$ solution models (**Fig. 9**).  We demonstrate this by comparing

548    our calculated activities with predictions from a Margules-like mixing model that

549    reasonably reflects the *ab initio* results (de Koker et al., 2013) at lower mantle pressures

550    (**Fig. 9**). Margules interaction parameters ($W_i$) in a asymmetric regular solution model

551    describe and fit the excess Gibbs free energy of the binary liquid mixture (e.g.

552    Thompson, 1967 and Haselton and Newton, 1980) as:

$$G_{mix} = G_{ideal} + W_A\, Y^2(1 - Y) + W_B\, Y(1 - Y)^2 \tag{7}$$

553    where $Y = \frac{X}{X + \lambda(1 - X)}$ and $X = X(SiO_2)$ (molar fraction of $SiO_2$) so that $X = Y$ when $\lambda = 1$.

554    However, de Koker et al. (2013) suggests using $\lambda = 1.43$, which allows for additional

555     asymmetry in $G_{mix}$ and enables a match to their low pressure enthalpy of mixing data.

556     The resulting Margules parameters for the binary mixture are the following:

$$W_A = 80 \cdot 10^3 - 70T \qquad\qquad (8)$$

$$W_B = -245 \cdot 10^3 - 25T \qquad\qquad (9)$$

557     In **Fig. 9** we observe the pressure-driven increase in the activity of $SiO_2$ derived from the

558     de Koker et al. (2013) endmembers and bridgmanite + stishovite eutectic temperatures,

559     and at face value the indication is that bridgmanite + stishovite eutectic melts become

560     markedly more $SiO_2$-rich. Such a dramatic change in the bridgmanite + stishovite

561     eutectic composition would require a rapid change in melt solution properties at high

562     pressures, which seems unlikely, and so a different explanation is required. We note that

563     the calculated increase in silica activity is a direct consequence of the marked flattening

564     of the de Koker et al. (2013) $SiO_2$ melting curve at high pressures (based on first-

565     principles simulations by Karki et al., 2007; **Fig. S2a**), which is not mirrored in the

566     pressure dependence of bridgmanite + stishovite eutectic temperatures presented in

567     this study. Our results may thus indicate that the melting curve and properties of $SiO_2$

568     melt require reassessment. Especially as a number of ab initio studies note that

569     obtaining accurate thermodynamic properties of silica-rich solids and liquid remains

570     challenging due to a high degree of polarization and very slow diffusion of viscous liquid

571     silica (e.g. Tangney and Scandolo, 2002).
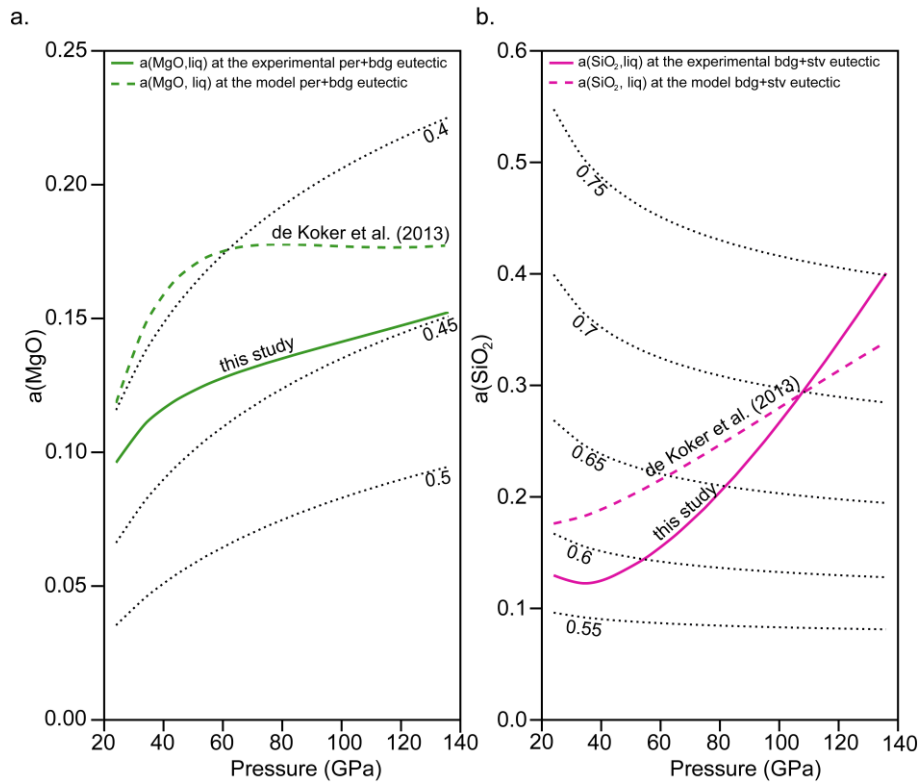
**Fig. 9.** A comparison between the activities of **(a)** MgO and **(b)** $SiO_2$ in eutectic liquids calculated based on the thermodynamic model of de Koker et al. 2013 using experimentally determined eutectic melting curves from this study (solid lines) compared with previous estimates (dashed lines) which reflects the variation of bridgmanite + periclase (green) and bridgmanite + stishovite (pink) eutectic compositions with pressure. The dotted lines are calculated for different melt compositions at the experimentally derived eutectic temperature, according to the modified Margules mixing model described in the main text.

Our experimental results also provide considerable constraints on the mixing properties of MgO-$SiO_2$ liquids. Specifically, the 100 – 500 K difference between the bridgmanite + periclase and bridgmanite + stishovite eutectic temperatures is a sensitive function of the shape of the free energy mixing curve. Although the results of de Koker et al. (2013) produce similar temperature differences between the eutectics, we note that this prediction is dependent on large entropies of mixing, coupled with a model in which bridgmanite is about 40 kJ/mol more stable relative to periclase + stishovite than in experimental datasets at 24 GPa (e.g. Stixrude and Lithgow-Bertelloni, 2011; Holland and Powell, 2011 **Fig. S2b**). If we assume instead that the experimentally

590 derived datasets provide accurate estimates of the free energy of the reaction

591 bridgmanite = periclase + stishovite, then our eutectic melting curves tell two things

592 about the mixing and endmember properties of the MgO-SiO$_2$ melt system. First, a low

593 temperature bridgmanite + stishovite eutectic (relative to bridgmanite + periclase)

594 indicates that SiO$_2$ melting temperatures are probably overestimated, at least at

595 pressures corresponding to shallow parts of the lower mantle. Second, to ensure that

596 melting of bridgmanite remains congruent despite a relatively low stability (relative to

597 its constituent oxides), the minimum in the liquid Gibbs free energy of mixing must be

598 quite angular and shifted to the MgO-rich side of bridgmanite. This angularity can be

599 explained by a maximum in short range order around the Mg$_2$SiO$_4$ composition, which

600 has been proposed on the basis of both theoretical considerations and low pressure

601 experimental results (Wu et al., 1993; Harvey et al., 2015). This maximum implies that

602 the activities of MgO and SiO$_2$ in ultramafic melts change quite abruptly as a function of

603 silica content, which could strongly influence phase equilibria in a partially molten

604 mantle.

**4.4 Implications for Melting in the Deep Mantle**

**4.4.1 Crystallization of a Deep Magma Ocean**

607 During the late stage accretion of Earth one or more giant impacts probably

608 resulted in deep magma ocean(s) on a global scale (e.g. Benz and Cameron, 1990).

609 Crystallization of a Hadean magma ocean would have set the initial state of the mantle,

610 with crystal-melt fractionation potentially leading to large-scale early mantle

611 heterogeneity. Near-equilibrium crystallisation of a magma ocean, as a result of efficient

612 convective mixing of suspended crystals, would not be an effective fractionation

613 mechanism (e.g. Solomotov and Stevenson, 1993). Fractional crystallization due to

614 crystal settling or floating, or liquid segregation and trapping due to negative buoyancy

615 could, however, lead to extensive primordial differentiation. The density contrast

between crystals and liquid is therefore a key parameter controlling magma ocean evolution. Another important factor is the depth at which the magma ocean begins to crystallize, which depends on the relationship between the magma ocean adiabatic temperature gradient and the slope of the peridotite liquidus.

First principles molecular dynamics simulations of melts in the $MgSiO_3$ system (Stixrude and Karki, 2005; Stixrude et al., 2009) show that the liquid adiabat, due to a continuous increase in the Gruneisan parameter of the liquid with pressure, is steeper than the melting curve, such that crystallization should begin in the middle of the lower mantle, rather than from the bottom up. On the basis of the shape of the bridgmanite + periclase eutectic curve found here, and assuming that the $MgSiO_3$ liquid adiabat is an adequate representation of the more MgO-rich eutectic liquid, the adiabat would intersect the melting curve at about 100 GPa (**Fig. 8a**). That is, our eutectic curve is consistent with crystallization beginning deep within a global magma ocean, but not at the bottom. However, the shape of the melting curve above 110 GPa is an extrapolation of the fit of the experimental data obtained at lower pressures.

A middle-outward style of crystallization creates the potential for residual melts to become trapped near the bottom of the lower mantle forming a 'basal magma ocean', the remnants of which may manifest themselves in the modern Earth as seismic low velocity structures (LLSVP, ULVZ) (e.g. Labrosse et al., 2007). The melt-solid density difference will determine the fate of the basal liquid. Petitgirard et al. (2015) measured the density of amorphous $MgSiO_3$ at high pressures, and predicted a very small density contrast between crystalline and molten bridgmanite. With the strong preference for iron to partition from ferropericlase and bridgmanite into melt relative to magnesium (e.g. Tateno et al., 2014; Pradhan et al., 2015; Boukaré et al., 2015) it is probable that a melt-solid density cross-over exists in the lower mantle, and that basal melt derived from mid-mantle magma ocean crystallisation would remain negatively buoyant.

### 4.4.2 Melting of Peridotite and Basalt at the CMB

642

643    The mantle adiabat by Anzellini et al. (2013) extended to an outermost core

644    temperature of 4050 K, is shown in **Fig. 8**. The bridgmanite + periclaseeutectic melting

645    curve (model peridotite) does not intersect the adiabat, so melting would not be

646    predicted to occur at the base of the modern mantle based on the simplified system. The

647    melting curves of Fiquet et al. (2010) and Andrault et al. (2011) also lie just above the

648    adiabat at the CMB, although within uncertainty. Only the melting curve of Nomura et al.

649    (2014) lies clearly below the adiabat such that melting at the base of the mantle is

650    predicted to occur.

651    In contrast, our bridgmanite + stishovite melting curve (model basalt) intersects

652    the mantle adiabat just above the core-mantle boundary, as do all melting curves for

653    natural basalt. This region above the CMB is where localised but significant reductions

654    in both P- and S- wave velocities are observed in seismic data (e.g. Williams and

655    Garnero, 1996, Garnero and Helmberger, 1998). Thus, partially molten recycled basalt is

656    considered a possible candidate material for the thin ultra-low velocity zones (ULVZs)

657    located directly above the outer core surface (e.g. Andrault et al., 2014; Pradhan et al.,

658    2015). Subducted oceanic crust is slightly denser than the ambient peridotite (e.g.

659    Ballmer et al., 2015) and may partially segregate downwards in the low-viscosity D"

660    zone during conductive heat transfer from the outer core and lateral flow towards the

661    LLSVPs (Torsvik et al., 2016). Basaltic material near the bottom of the D" flow may

662    interact and replenish the ULVZs, which are frequently confined to LLSVP-margins (e.g.

663    Thorne and Garnero, 2004).  Moreover, most deep plumes seem to be rooted near the

664    edges of the LLSVPs and therefore may partially entrain basaltic material from the

665    ULVZs (French and Romanowicz, 2015; Torsvik et al., 2016).

### 5. Conclusions

666

Eutectic phase relations in the system $MgO$-$SiO_2$ involving the assemblages bridgmanite + periclase + melt and bridgmanite + stishovite + melt provide analogues for melting of peridotite and basalt at lower mantle conditions, respectively. Our experimental melting curves from ~20-110 GPa provide constraints on the maximum melting temperatures in peridotitic and basaltic lithologies relevant to the Earth's mantle. The bridgmanite + periclase (peridotite) melting curve is ~100 K higher at the top of the mantle than the bridgmanite + stishovite (basalt) melting curve, but is ~500 K higher at the CMB. The bridgmanite + periclase eutectic curve has a shape indicating that a deep, peridotitic global magma ocean would begin crystallizing at ~100 GPa, favouring the possibility of residual, basal melt layer at the base of the mantle. Relative to estimates of the mantle geotherm, our data indicate that basalt will melt near the core-mantle boundary. The model peridotite eutectic is about 500 K higher than the mantle geotherm at the core-mantle boundary, but melting may occur due to the depression of the solidus caused by additional components (e.g. $FeO$, $CaO$, $Al_2O_3$, $Na_2O$).

**Acknowledgements**

**References**

Alfé D., 2005. Melting Curve of MgO from First-Principles Simulations. Phys. Rev. Lett. 94, 235701.

Anzellini, S., Dewaele, A., Mezouar, M., Loubeyre, P., Morard, G., 2013. Melting of iron at Earth's inner core boundary based on fast X-ray diffraction. Science 340 (6131), 464-466.

Andrault, D., Bolfan-Casanova, N., Nigro, G.L., Bouhif, M.A., Garbarino, G., Mezouar, M., 2011. Melting curve of the deep mantle applied to properties of early magma ocean and actual core-mantle boundary. Earth Planet. Sci. Lett. 304, 251-259.

Andrault, D., Pesce G., Bouhifd, M.A., Bolfan-Casanova, N., Hénot, J.-M., Mezouar, M., 2014. Melting of subducted basalt at the core-mantle boundary. Science 344 (6186), 892-895.

Ballmer, M.D., Schmerr, N.C., Nakagawa, T., Ritsema, J., 2015. Compositional mantle layering revealed by slab stagnation at ~1000-km depth. Sci. Adv. 1, 1-9.

Benz W., Cameron A., G., H., 1990. Terrestrial effects of the Giant Impact. In: Newsom HE & Jones JH (eds.), New York: Oxford University Press, Origin of the Earth, 61-67.

Boukaré, C.-E., Ricard, Y., Fiquet, G., 2015. Thermodynamics of the MgO-FeO-SiO2 system up to 140 GPa : application to the crystallization of Earth's magma ocean. J. Geophys. Res. Solid Earth 120, 6085-6101.

Campbell, A.J., 2008. Measurement of temperature distributions across laser heated samples by multispectral imaging radiometry. Rev. Sci. Instrum. 79, 015108.

de Koker, N., Strixrude, L., 2009. Self-consistent thermodynamic description of silicate liquids, with application to shock melting of MgO periclase and $MgSiO_3$ perovskite. Geophys. J. Int. 178, 162–179.

de Koker, N., Karki, B.B., Stixrude, L., 2013. Thermodynamics of the $MgO–SiO_2$ liquid system in Earth's lowermost mantle from first principles. Earth Planet. Sci. Lett. 361, 58-63.

Di Paola, C., Brodholt, J.P., 2016. Modeling the melting of multicomponent systems: the case of $MgSiO_3$ perovskite under lower mantle conditions. Sci. Rep. 6, 29830.

722  Dziewonski, A.M., Anderson, D.L., 1981. Preliminary reference Earth model. Phys. Earth
723  Planet. Inter. 25(4), 297-356.

724  Fiquet, G., Auzende, A.L., Siebert, J., Corgne, A., Bureau, H., Ozawa, H., Garbarino, G., 2010.
725  Melting of peridotite to 140 GPa. Science 329, 1516-1518.

726  French, S.W., Romanowicz, B., 2015. Broad plumes rooted at the base of the Earth's
727  mantle beneath major hotspots. Nature 525, 95–99.

728  Garnero, E.J., Helmberger, D.V., 1998. Further structural constraints and uncertainties of
729  a thin laterally varying ultralow-velocity layer at the base of the mantle. J. Geophys. Res.
730  103 (B6), 12495-1250.

731  Garnero, E.J., McNamara, A.K., 2008. Structure and dynamics of Earth's lower mantle.
732  Science 230, 626-628.

733  Gasparik, T., 1990. Phase relations in the transition zone. J. Geophys. Res. 95, 15751-
734  15769.

735  Geballe, Z.M., Jeanloz, R., 2012. Origin of temperature plateaus in laser-heated diamond
736  anvil cell experiments. J. Appl. Phys. 111, 123518-1-15.

737  Hanfland, M., Syassen, K., Fahy, S., Louie, S.G., Cohen, M.L., 1986. The 1st-order Raman
738  mode of diamond under pressure. Physica B+C, 139 & 140B, 516-519.

739  Harvey, J.-P., Gheribib, A.E., Paul D. Asimow, P.D., 2015. A self-consistent optimization of
740  multicomponent solution properties: Ab initio molecular dynamic simulations and the
741  $MgO–SiO_2$ miscibility gap under pressure. Geochim. Cosmochim. Acta 161, 146–165.

742  Haselton, H.T., Newton, R.C., 1980. Thermodynamics of pyrope-grossular garnets and
743  their stabilities at high temperatures and high pressures. J.Geophys.Res. 85, 697306982.

744  Helffrich, G., 2006. Small-scale seismic heterogeneity and mantle structure. Astron.
745  Geophys. 47, 1.20-1.26.

746  Hirose, K., Fei, Y., Ma, Y., Mao, H.-K., 1999. The fate of subducted basaltic crust in the
747  Earth's lower mantle. Nature 397, 53-56.

748  Holland, T.J.B., Powell, P., 2011. An improved and extended internally consistent
749  thermodynamic dataset for phases of petrological interest, involving a new equation of
750  state for solids. J. Metamorph. Geol. 29, 333–383.

751 Karki, B.B., Bhattarai, D., Stixrude, L., 2007. First-principles simulations of liquid silica:
752 structural and dynamical behavior at high pressure. Phys. Rev. B, 76, 104205.

753 Labrosse, S., Hernlund, J.W., Coltice, N., 2007. A crystallizing dense magma ocean at the
754 base of the Earth's mantle. Nature 450, 866-869.

755 Lay, T., Hernlund, J., Buffett, B.A., 2008. Core-mantle boundary heat flow. Nat. Geosci. 1,
756 25-32.

757 Liebske, C., Corgne, A., Frost, D.J., Rubie, D.C. and Wood, B.J., 2005. Compositional effects
758 on element partitioning between Mg-perovskite and silicate melts. Contributions to
759 Mineralogy and Petrology 149, 113-128.

760 Liebske, C., Frost, D.J., 2012. Melting phase relations in the $MgO–MgSiO_3$ system between
761 16 and 26 GPa: Implications for melting in Earth's deep interior. Earth Planet. Sci. Lett.
762 345-348, 159–170.

763 Lord, O.T., Wann, E.T.H., Hunt, S.A., Walker, A.M., Santangeli, J., Walter, M.J., Dobson, D.P.,
764 Wood, I.G., Vočadlo, L., Morard, G., Mezouard, M., 2014a. The NiSi melting curve to 70
765 GPa. Phys. Earth Planet. Inter. 233, 13-23.

766 Lord, O. T., Wood, I. G., Dobson, D. P., Vočadlo, L., Wang, W., Thomson, A. R., et al. 2014b.
767 The melting curve of Ni to 1 Mbar. Earth Planet. Sci. Lett. 408, 226–236.

768 Mao, H.K., Xu, J., Bell, P.M., 1986. Calibration of the ruby pressure gauge to 800-kbar
769 under quasi-hydrostatic conditions. J. Geophys. Res. Solid Earth 91, 4673-4676.

770 McNamara, A., K., Zhong, S., 2005. Thermochemical structures beneath Africa and the
771 Pacific Ocean. Nature 437, 1136–1139.

772 Murakami, M., Ohishi, Y., Hirao, N., Hirose, K., 2012. A perovskitic lower mantle inferred
773 from high-pressure, high-temperature sound velocity data. Nature 485, 90–94.

774 Nakagawa, T., Tackley, P.J., 2008. Lateral variations in CMB heat flux and deep mantle
775 seismic velocity caused by a thermal-chemical-phase boundary layer in 3D spherical
776 convection, Earth Planet. Sci. Lett. 271, 348-358.

777 Nomura, R., Hirose, K., Uesugi, K., Ohishi, Y., Tsuchiyama, A., Miyake, A., Ueno, Y., 2014.
778 Low core-mantle boundary temperature inferred from the solidus of pyrolite. Science,
779 343, 522-525.

780 Petitgirard S., Malfait, W.J., Sinmyo, R., Kupenko, I., Hennet, L., Harries, D., Dane, T.,
781 Burghammer, M., Rubie, D.C., 2015. Fate of $MgSiO_3$ melts at core–mantle boundary
782 conditions. PNAS 112 (46), 14186–14190.

783 Pradhan, G.K., Fiquet, G., Siebert, J., Auzendea, A.-L., Morard, G., Antonangeli, D.,
784 Garbarino, G., 2015. Melting of MORB at core–mantle boundary. Earth Planet. Sci. Lett.
785 431, 247-255.

786 Presnall, D.C., Walter, M.J., 1993. Melting of forsterite, $Mg_2SiO_4$, from 9.7 to 16.5 GPa. J.
787 Geophys. Res. 98, B 11, 19,777-19,78.

788 Presnall, D.C., Weng, Y.-H., Milholland, C.S., Walter, M.J., 1998. Liquidus phase relations in
789 the system $MgO–MgSiO_3$ at pressures up to 25 GPa - constraints on crystallization of a
790 molten Hadean mantle. Phys. Earth Planet. Inter. 107 (1–3), 83–95.

791 Simon, F.E., Glatzel, G.Z., 1929. Remarks on fusion pressure curve. Zeitschrift für
792 Anorganische und Allgemeine Chemie, 178, 309-312.

793 Sinmyo, R., Hirose, K., 2010. The Soret diffusion in laser-heated diamond anvil cell. Phys.
794 Earth Planet. Inter. 180, 172-178.

795 Shen, G., Lazor, P., 1995. Measurement of melting temperatures of some minerals under
796 lower mantle pressures. J. Geophys. Res. 100 (B9), 17699-17713.

797 Solomatov, V. S., Stevenson, D. J., 1993. Kinetics of crystal growth in a terrestrial magma
798 ocean. J. Geophys. Res. 98 (E3), 5407-5418.

799 Stixrude, L., Karki, B.B., 2005. Structure and freezing of $MgSiO_3$ liquid in Earth's lower
800 mantle. Science 310, 297-299.

801 Stixrude, L., de Koker, N., Sun, N., Mookherjee, M., Karki, B.B., 2009. Thermodynamics of
802 silicate liquids in the deep Earth. Earth Planet. Sci. Lett. 278, 226–232.

803 Stixrude, L., Lithgow-Bertelloni C., 2011. Thermodynamics of mantle minerals - I.
804 Physical properties. Geophys. J. Int., 162, 610–632.

805 Tangney, P., Scandolo, S., 2002. An *ab initio* parametrized interatomic force field for
806 silica, J. Chem. Phys. 117, 8898-8904.

807 Tateno, S., Hirose, K., Ohishi, Y., 2014. Melting experiments on peridotite to lowermost

808 mantle conditions. J. Geophys. Res. Solid Earth 119, 4684-4694.

809 Thomas, C. W., Asimow, P. D., 2013. Preheated shock experiments in the molten

810 $CaAl_2Si_2O_8$-$CaFeSi_2O_6$-$CaMgSi_2O_6$ ternary: A test for linear mixing of liquid volumes at

811 high pressure and temperature. J. Geophys. Res. Solid Earth 118, 3354-3365.

812 Thompson, J.B. Jr., 1967. Thermodynamic properties of simple solutions. In: Researches

813 in Geochemistry (ed. Ableson, P.H.). New York, Wiley and Sons, 340 – 361.

814 Thomson, A.R., Walter, M.J., Lord, O.T., Kohn, S.C., 2014. Experimental determination of

815 melting in the system enstatite-magnesite and magnesite-calcite from 15 to 80 GPa. Am.

816 Mineral. 99, 1544-1554.

817 Thorne, M.S., Garnero, E.J., 2004. Inference on ultralow-velocity zone structure from a

818 global analysiss of SPdKS waves. J. Geophys. Res. B, 109, B08302:1-22.

819 Torsvik, T.H., Steinberger, B., Ashwal, L.D., Doubrovine, P.V., Trønnes, R.G., 2016. Earth

820 evolution and dynamics – a tribute to Kevin Bruke. Can. J. Earth Sci., 53, 1073-1087.

821 Trønnes, R.G., Frost, D.J., 2002. Peridotite melting and mineral-melt partitioning of major

822 and minor elements at 22–24.5 GPa. Earth Planet. Sci. Lett. 197, 117-131.

823 Walter, M.J., Koga, K.T., 2004. The effects of chromatic dispersion on temperature

824 measurement in the laser-heated diamond anvil cell. Phys. Earth Planet. Inter. 143 and

825 144, 541-558.

826 Walter, M.J., Nakamura, E., Trønnes, R.G., Frost, D., 2004. Experimental constraints on

827 crystallization differentiation in a deep magma ocean. Geochim. Cosmochim. Acta 68

828 (20), 4267 - 4284

829 Walter, M.J., Thomson, A.R., Wang, W., Lord, O.T., Ross, J., McMahon, S.C., Baron, M.A.,

830 Melekhova, E., Kleppe, A.K., Kohn, S.C., 2015. The stability of hydrous silicates in Earth's

831 lower mantle: experimental constraints from the systems $MgO$-$SiO_2$-$H_2O$ and $MgO$-$Al_2O_3$-

832 $SiO_2$-$H_2O$. Chem. Geol. 418, 16-29.

833 Williams, Q., Garnero, E.J., 1996. Seismic evidence for partial melt at the base of earth's

834 mantle. Science, 273(5281), 1528-1530.

835  Wu, P., Eriksson, G., Peltonand, A. D., Blander, M., 1993. Prediction of the
836  Thermodynamic Properties and Phase Diagrams of Silicate Systems – Evaluation of the
837  FeO-MgO-Si0$_2$ System. ISIJ Int. 33 (1), 26-35.

838  Zerr, A., Boehler, R., 1993. Melting of (Mg,Fe)SiO$_3$-perovskite to 625 kilobars: Indication
839  of a high melting temperature in the lower mantle. Science 262, 553-555.

840

841

842

843

844

845

846

847

848

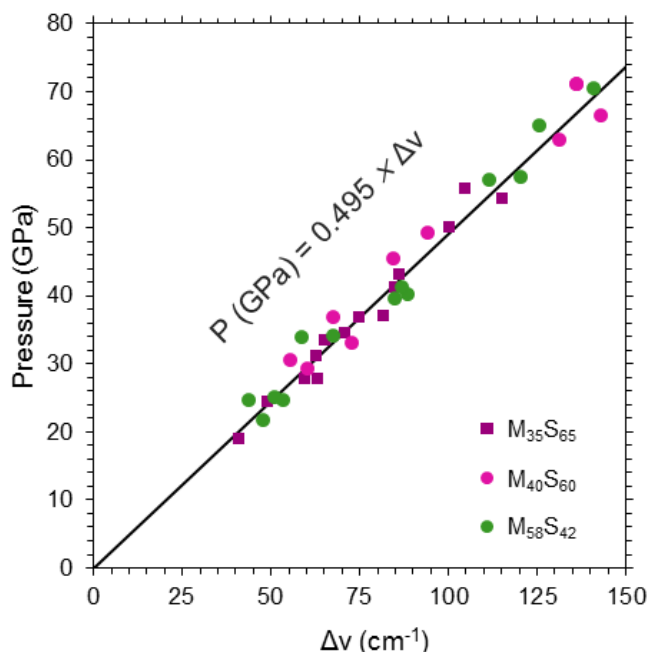849

850

851

852

853

854

855

856

857

858

859

860

861

862

## Supplementary materials

864



865

**Figure S1.** Calibration of the stress-induced Raman shift of the diamond singlet mode measured at the culet surface relative to pressure measured by ruby fluorescence, both measured after quenching. To calibrate the diamond peak shift, ruby was added to one of the sample chambers in many of our multi-chamber experiments. After laser heating we measured both the R1 ruby fluorescence peak from the ruby-bearing sample chamber and the Raman shift of the singlet peak from the diamond culet at the same position. Thomson et al. (2014) and Walter et al. (2015) found that the calibration can vary depending on the sample material and pressure media, therefore separate calibration curves for the different compositions were tested. The linear regressions for MgO-rich and $SiO_2$-rich samples resulted in slopes of 0.4937 and 0.4954 GPa/(cm)$^{-1}$, respectively, and are within uncertainty, therefore we fitted all the data points simultaneously yielding a slope of 0.495 GPa/(cm)$^{-1}$ when forced through the origin.
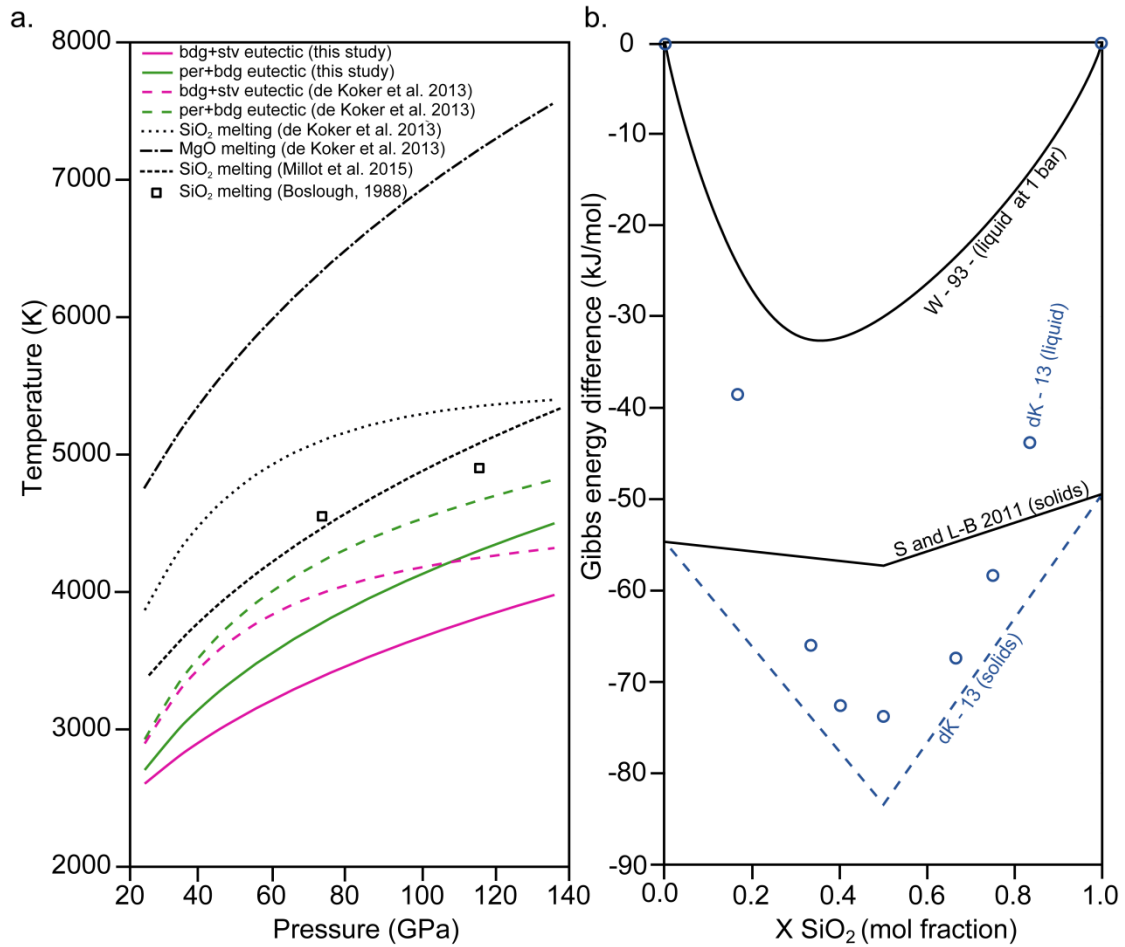
878

879

880

881

882

883

**Figure S2. (a)** The per + bdg (green solid line) and bdg + stv (pink solid line) eutectic melting curves experimentally determined in this study and ab initio results by de Koker et al. (2013; dashed lines) together with MgO and $SiO_2$ melting curves used in the thermodynamic modelling by de Koker et al. (2013) and our calculations of MgO and $SiO_2$ activities in the liquids. The endmembers melting curves were originally determined by Koker and Stixrude (2009) and Karki et al. (2006) for MgO and Karki et al. (2007) for $SiO_2$. Recently determined melting curve for $SiO_2$ based on shock data extended to 500 GPa by Millot et al. (2015) and previous shock data by Boslough, 1988 suggests lower and steeper melting curve of $SiO_2$. **(b)** The difference in Gibbs energy of solids and liquids at 24 GPa and 2605 K from de Koker et al. (2013) (dK - 13) study in comparison with experimental datasets for solids by Stixrude and Lithgow-Bertelloni (2011) (S and L-B - 2011) and 1 bar experimental liquid Gibbs free energy of mixing curve from Wu et al. (1993) (W - 93).

901

902

**Table S1.** Experimental conditions and melting temperatures (K) in the MgO-MgSiO$_3$ sub-system.

| C | Experiment | P (GPa) | T$_{max}$ | σ | T$_{max,s}$ | σ |
|---|---|---|---|---|---|---|
| M$_{58}$S$_{42}$ | MB_E4_A | 30,7 | 2831 | 65 | 2793 | 65 |
| | MB_E4_D | 44,3 | 3304 | 185 | 3323 | 184 |
| | MB_E4_C | 50,0 | 3603 | 91 | 3506 | 93 |
| | MB_E9_A | 20,4 | 2734 | 109 | 2705 | 161 |
| | MB_E9_C | 55,7 | 3509 | 15 | 3502 | 14 |
| | MB_E10_D | 32,7 | 3145 | 50 | 3142 | 50 |
| | MB_E16_D | 27,4 | 2782 | 101 | 2770 | 98 |
| | MB_E18_A | 35,4 | 3112 | 60 | 3071 | 63 |
| | MB_E18_B | 40,3 | 3193 | 56 | 3174 | 62 |
| | MB_E18_C | 47,8 | 3448 | 166 | 3433 | 156 |
| | MB_E32 | 99,1 | 4161 | 131 | 4072 | 130 |
| | MB_E33_A | 69,8 | 3687 | 103 | 3637 | 112 |
| | MB_E33_C | 63,6 | 3630 | 91 | 3617 | 93 |
| | MB_E33_B | 77,4 | 4004 | 118 | 4013 | 175 |
| | MB_E43_C | 48,2 | 3164 | 57 | 3150 | 101 |
| | MB_E43_B | 54,1 | subsolidus ~2400 K | | | |
| | MB_E43_A | 58,0 | subsolidus ~2150 K | | | |
| | MB_E43_D | 50,7 | long subsolidus ~1800 K (30 minutes) | | | |
| | MB_E48_C | 58,2 | 3556 | 89 | 3484 | 93 |
| | MB_E48_A | 63,3 | subsolidus ~2450 K | | | |
| | MB_E48_B | 60,0 | long subsolidus ~2200 (30 minutes) | | | |
| | MB_E50_C | 40,1 | 3324 | 108 | 3291 | 102 |
| | MB_E50_A | 47,3 | subsolidus ~2500 K | | | |
| | MB_E50_B | 45,0 | subsolidus ~2400 (30 minutes) | | | |

903

904

905

906

907

908

909

910

911

912

913

914

**Table S2.** Experimental conditions and melting temperature (K) in the MgSiO$_3$–SiO$_2$ sub-system

| C | Experiment | P (GPa) | T $_{max}$ | σ | T $_{max,s}$ | σ |
|---|---|---|---|---|---|---|
| | MB_E3_C | 28,6 | 2757 | 36 | 2753 | 35 |
| | MB_E5_A | 23,1 | 2645 | 109 | 2640 | 108 |
| | MB_E5_D | 42,5 | 3112 | 94 | 3102 | 93 |
| | MB_E5_C | 45,3 | 2796 | 72 | 2784 | 47 |
| | MB_E7_A | 32,3 | 3004 | 45 | 2997 | 45 |
| | MB_E29 | 108,5 | 3887 | 156 | 3852 | 271 |
| | MB_E34 | 89,3 | 3448 | 289 | 3449 | 274 |
| | MB_E37 | 91,4 | 3690 | 299 | 3675 | 304 |
| | MB_E44_C | 48,3 | 3038 | 186 | 3026 | 178 |
| | MB_E44_B | 53,3 | subsolidus ~2350 K | | | |
| | MB_E44_A | 49,1 | subsolidus ~2300 K | | | |
| | MB_E44_D | 44,8 | long subsolidus ~2000 K (30 minutes) | | | |
| M$_{35}$S$_{65}$ | MB_E47_B | 80,0 | subsolidus ~2900 K | | | |
| | MB_E47_C | 86,1 | subsolidus ~2450 K | | | |
| | MB_E47_A | 78,3 | long subsolidus ~2200 K (30 minutes) | | | |
| | MB_E8_D | 30,6 | 2910 | 42 | 2894 | 38 |
| | MB_E8_A | 55,2 | 3066 | 74 | 3055 | 70 |
| | MB_E8_B | 67,0 | 3188 | 44 | 3162 | 39 |
| | MB_E8_C | 68,7 | 3472 | 42 | 3444 | 40 |
| | MB_E11_A | 21,7 | 2497 | 120 | 2486 | 115 |
| | MB_E11_D | 29,3 | 2719 | 128 | 2669 | 203 |
| | MB_E11_B | 43,7 | 2938 | 121 | 2930 | 124 |
| | MB_E12_D | 30,1 | 2982 | 82 | 2949 | 78 |
| | MB_E12_B | 51,3 | 3281 | 123 | 3269 | 116 |
| | MB_E19_C | 35,4 | 2938 | 323 | 2916 | 312 |
| | MB_E19_A | 77,2 | 3479 | 181 | 3468 | 177 |
| | MB_E19_B | 73,7 | 3151 | 60 | 3144 | 58 |
| | MB_E22_A | 42,7 | 2968 | 115 | 2957 | 112 |
| | MB_E22_B | 60,2 | 3334 | 105 | 3312 | 105 |
| | MB_E36_A | 37,8 | 2775 | 146 | 2760 | 141 |
| | MB_E36_C | 36,7 | subsolidus ~2500 K | | | |
| | MB_E36_B | 53,1 | subsolidus ~2700 K | | | |
| | MB_E49_B | 62,3 | subsolidus ~2900 K | | | |
| | MB_E49_A | 71,8 | subsolidus ~2400 K | | | |
| | MB_E49_C | 68,0 | long subsolidus ~2700 K (30 minutes) | | | |
| | MB_E45_A | 80,1 | 3625 | 51 | 3573 | 45 |
| M$_{40}$S$_{60}$ | MB_E45_B | 80,8 | subsolidus ~2400 K | | | |
| | MB_E45_C | 81,3 | long subsolidus ~2000 K (30 minutes) | | | |

915

916

917

918

**Table S3.** Fitting parameters for the melting curves defined in this study

| eutectic: | $T_{24}$ (K) | $A$ (GPa) | | $C$ |
|---|---|---|---|---|
| MgO-MgSiO$_3$ | 2705 | 19.156 ± 7.38 | 3.7796 ± 0.878 | |
| MgSiO$_3$-SiO$_2$ | 2605 | 29.892 ± 16.2 | 3.6770 ± 1.28 | |

The Simon-Glatzel equation: $T_m = T_{24}\left(1 + \frac{P_m}{A}\right)^{\frac{1}{C}}$ (Simon and Glatzel, 1929)

919

920  **References:**

921  Boslough, M.B., 1988. Postshock temperatures in silica. J. Geophys. Res. 93 (B6), 6477-
922  6484.

923  de Koker, N., Strixrude, L., 2009. Self-consistent thermodynamic description of silicate
924  liquids, with application to shock melting of MgO periclase and MgSiO$_3$ perovskite.
925  Geophys. J. Int. 178, 162–179.

926  de Koker, N., Karki, B.B., Stixrude, L., 2013. Thermodynamics of the MgO–SiO$_2$ liquid
927  system in Earth's lowermost mantle from first principles. Earth Planet. Sci. Lett. 361, 58-
928  63.

929  Karki, B.B., Bhattarai, D., Stixrude, L., 2006. First principles calculations of the structural,
930  dynamical and electronic properties of liquid MgO. Phys. Rev. B 73, 174208.

931  Karki, B.B., Bhattarai, D., Stixrude, L., 2007. First-principles simulations of liquid silica:
932  structural and dynamical behavior at high pressure. Phys. Rev. B 76, 104205.

933  Millot, M., Dubrovinskaia, N., Černok, A., Blaha, S., Dubrovinsky, L., Braun, D.G., Celliers,
934  P.M., Collin, G.W., Eggert, J.H., Jeanloz, R., 2015. Shock compression of stishovite and
935  melting of silica at planetary interior conditions. Science 418, 8–11.

936  Simon, F.E., Glatzel, G.Z., 1929. Remarks on fusion pressure curve. Zeitschrift für
937  Anorganische und Allgemeine Chemie, 178, 309-312.

938  Stixrude, L., Lithgow-Bertelloni, C., 2011. Thermodynamics of mantle minerals - I.
939  Physical properties. Geophys. J. Int., 162, 610–632.

940   Thomson, A.R., Walter, M.J., Lord, O.T., Kohn, S.C., 2014. Experimental determination of
941   melting in the system enstatite-magnesite and magnesite-calcite from 15 to 80 GPa. Am.
942   Mineral. 99, 1544-1554.

943   Walter, M.J., Thomson, A.R., Wang, W., Lord, O.T., Ross, J., McMahon, S.C., Baron, M.A.,
944   Melekhova, E., Klepp, A.K., Kohn, S.C., 2015. The stability of hydrous silicates in Earth's
945   lower mantle: experimental constraints from the systems $MgO-SiO_2-H_2O$ and $MgO-Al_2O_3-$
946   $SiO_2-H_2O$. Chem. Geol. 418, 16-29.

947   Wu, P., Eriksson, G., Peltonand, A.D., Blander, M., 1993. Prediction of the Thermodynamic
948   Properties and Phase Diagrams of Silicate Systems – Evaluation of the $FeO-MgO-SiO_2$
949   System. ISIJ Int. 33 (1), 26-35.